

Aide mémoire for g-mode search

B.Andersen, T.Appourchaux, W.Finsterle, C.Fröhlich,

D.O.Gough, J.Provost, T.Toutain, T.Sekii, P.Scherrer

October 19, 1998

Abstract

This aide mémoire summarizes the joint effort of the SOI/MDI and VIRGO team for discovering g modes. The data sets and their reduction are described. The different technique used for detecting g modes are described. A list of g- and p-mode frequencies are given for 2 different models.

1 Introduction

Obviously the goal of the workshop was to detect the g modes. But as mentionned by D.O.Gough: *'It is superficially unfortunate that we discovered no g modes. On the brighter side, on which I always prefer to be, it shows that we have before us a greater challenge which will yield [] greater satisfaction when we overcome it.[...]. We are all now much more prepared to continue the search.'*

From now on this will be the motto of the g-mode group.

2 Data utilized

2.1 SOI/MDI velocity

The conversion from level 0 to level 1 data is explained in MDI/SOI Data Flow (Ver 0.54, 14 Feb 95). This is repeated here as a basis for the up-to-

date conversion (**Phil that is for you!**). Level 1 processing takes the level 0 product and

- performs calibration corrections,
- removes instrumental effects (Michelson temperature...),
- corrects for the flat field,
- applies look-up table corrections
- and converts the DN to calibrated engineering data.

If different flat field, calibration or DN conversion corrections are used, please Phil specify!

The level 1.4 are derived from level 1 by:

- making data evenly spaced,
- sub-sampling the data,
- grouping the input data series,
- gathering information from ancillary databases,
- allowing multiple variables.

MDI dataset is the level-1.4 LOI velocity proxy (180 pixels) from 1 May 1996 to 30 April 1997. Data with bad quality flag are put to 0. They are corrected from the satellite velocity and the offset due to tuning of the MDI. Then they are detrended using a third order polynomial this separately for each piece of signal in-between two changes of offset. An (l, m) spherical harmonic mask with $B = 0$ is applied to the data the resulting timeseries is high-pass filtered using a box-car smooth with a 1-day width. Data are then Fourier transformed.

2.2 SOI/MDI intensity

The level-1.4 LOI intensity proxy (180 pixels) was converted to a 12-pixel LOI proxy taking into account the number of CCD pixels in each sub pixel. Each pixel is then detrended using a 2-day triangle smoother. The relative variations are then computed and spikes larger than 5-7 sigma are removed. The 12 pixels are combined using the routines developed for the VIRGO/LOI. Time-independent spherical harmonics filters are applied to the 12 pixels to derive the signals for $l = 0$ to 6. The resulting spectra are heavily polluted by harmonics of 96 minutes and of $52 \mu\text{Hz}$. We found that the most efficient way to remove these spurious peaks was to subtract temporally the mean over the 12 pixels. This is of course at the expense of reducing the sensitivity of the SOI/MDI intensity signal to very low degree modes for which $l + m$ is even. The time series used starts on 23 May 1996 and ends on 16 September 1997.

2.3 VIRGO/SPM

The SPM data are based on the level 1 time series from 26 March 1996 (MD116) until 16 September 1997 (MD655). A running mean detrending of triangular shape and base width of two days was applied before computing the Fourier transform.

2.4 VIRGO/PMO6

The PMO6 data are based on the level 1 time series from 26 March 1996 (MD116) until 16 September 1997 (MD655). A running mean detrending of triangular shape and base width of two days was applied before computing the Fourier transform.

2.5 VIRGO/LOI

The LOI data are the level 1 data as reduced per VIR-SSD-GSE/L-001, (Ver 1.7, May 1996) from the level 0 data. It is available from the VIRGO home page. The LOI data are reduced in the same way as the SOI/MDI data except that there is no need to remove the 12-pixel average. The time series starts on 27 March 1996 and ends on 16 September 1997.

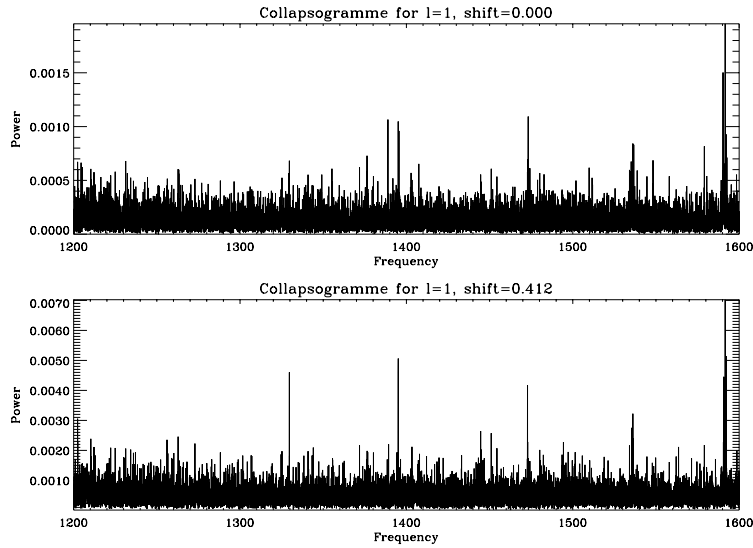


Figure 1: The central peak is an $l = 2$, $n = 8$. The 2 peaks on either side are $l = 1$, $n = 8, 9$.

3 Detection techniques

3.1 Collapsogramme

This is a very simple technique. It is based on the fact if the g modes exist they should be splitted by rotation. To enhance the presence of the modes that could be hidden in the noise, we decided to add the $2l+1$ power spectra (available from resolved instruments) after having shifted in frequency each of them by $m\Omega$, where m is the azimuthal order and Ω is the rotational splitting. The technique can of course be used for different Ω .

Any technique for detecting g modes should allow us to detect similarly low frequency p modes with very long lifetime. The technique used here has been applied succesfully to the SOI/MDI velocity data (Fig 1 to 6).

3.2 Bo-you-name-it technique

BA

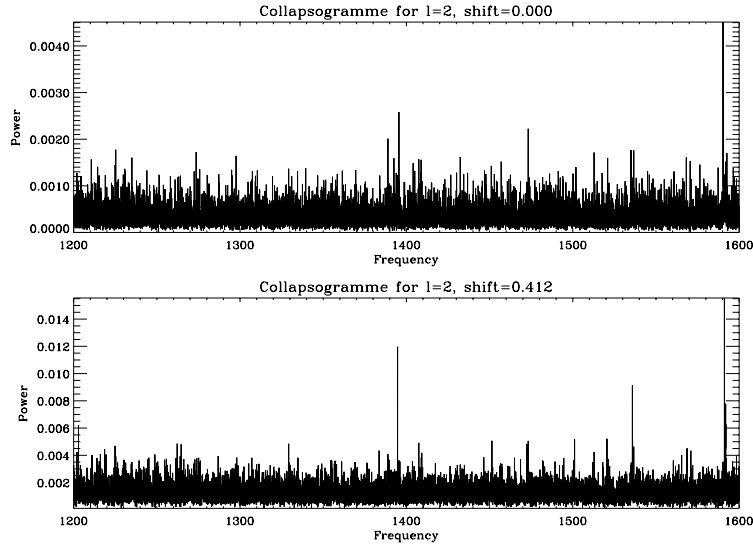


Figure 2: The central peak is an $l = 2, n = 8$.

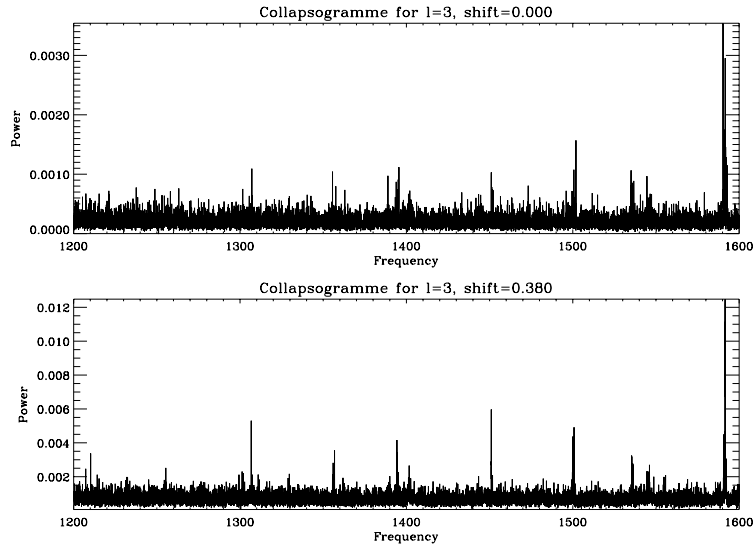


Figure 3: The peak close to $1300 \mu\text{Hz}$ is an $l = 3, n = 7$, and at $1450 \mu\text{Hz}$ an $l = 3, n = 8$. The peak close to $1210 \mu\text{Hz}$ is an $l = 4, n = 6$, and close to $1350 \mu\text{Hz}$ is an $l = 4, n = 7$.

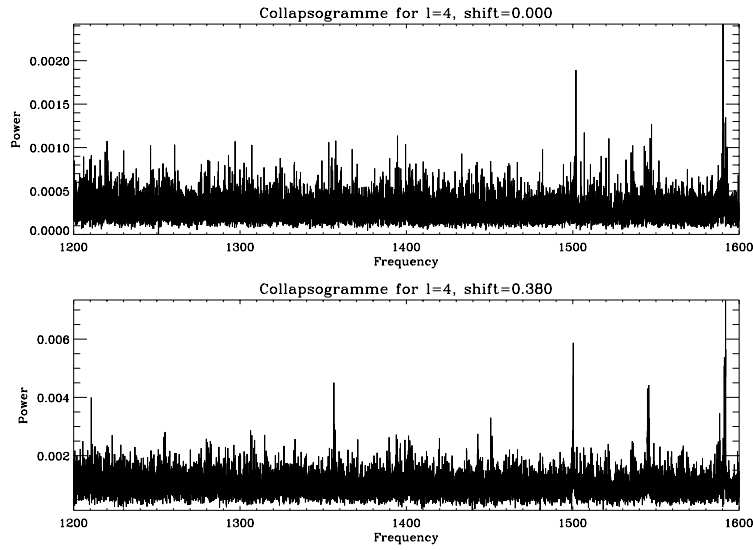


Figure 4: The peak close to 1210 μHz is an $l = 4$, $n = 6$, and close to 1350 μHz is an $l = 4$, $n = 7$.

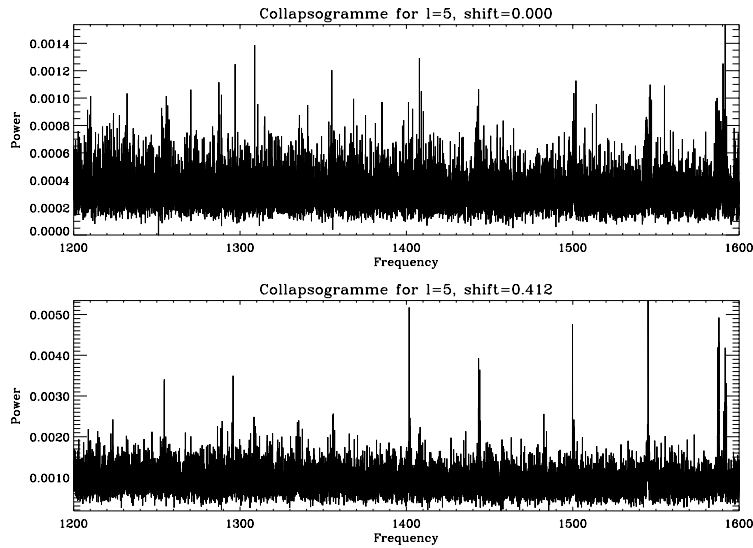


Figure 5: The peak close to 1250 μHz is an $l = 5$, $n = 6$, and at 1400 μHz an $l = 5$, $n = 7$.

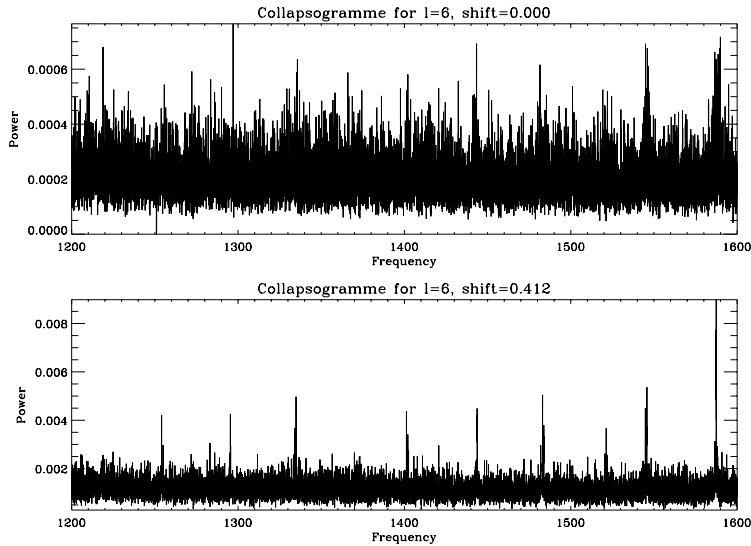


Figure 6: The peak close to 1300 μHz is an $l = 6$, $n = 6$, and at 1450 μHz an $l = 6$, $n = 7$.

3.3 Noise reduction techniques

We attempted to reduce instrumental noise by combining the Fourier spectra of the three SPM channels and the PMO6. We hoped that the summed spectra would have less noise because of the random phases which would cancel each other. The result was negative in the sense that the noise of the different channels and instruments did not cancel but turned out to be coherent. We therefore believe that the noise in the SPM and PMO6 spectra is mainly of solar origin.

Another attempt to reduce noise (instrumental or solar) was the following: We divided the time series into halfway overlapping parts of 100-200 days length. We calculated the power spectra of these parts and averaged them. Then two different methods to detect doublets were applied. The first was simply autocorrelation of the g modes range of the averaged spectrum.

The second method was very similar to the autocorrelation but without summing over the product of the original and the shifted spectra. The result is a sort of "frequency dependent" autocorrelation coefficient. The advantage of this method is that it returns high autocorrelation coefficients even if there

are only very few (or even one single) doublets. The results of both of these methods were negative.

4 Multivariate analysis

4.1 Parameters of Multivariate Spectral Regression Analysis

The multivariate regression analysis is trying to explain the dependent components, a q -dimensional vector $\mathbf{Y}(t)$, by filtered independent components, a p -dimensional vector $\mathbf{X}(t)$. Thus the following equation has to be solved, similar to the linear regression analysis

$$\mathbf{Y}(t) = \mathbf{L}(\mathbf{X}(t)) + \eta(t) \quad (1)$$

where \mathbf{L} is a multivariate linear filter with unknown $(q \times p)$ -dimensional transfer function $\mathbf{B}(\lambda)$ and $\eta(t)$ an unobservable q -dimensional process uncorrelated with $\mathbf{X}(t)$. The extent of the deviation of $\mathbf{Y}(t)$ from a linear function of $\mathbf{X}(t)$ is measured by the unknown spectral density matrix $\mathbf{f}^\eta(\lambda)$. This matrix and the transfer function $\mathbf{B}(\lambda)$, which indicates how the linear dependence is parcelled out to the various input and output series, are the principle parameters of interest. They are determined by minimizing

$$E(X_j(t) - Y_j(t))^2. \quad (2)$$

From this the transfer function of \mathbf{L} and the spectral density function of $\eta(t)$ can be calculated according to

$$\mathbf{B}(\lambda) = \mathbf{f}^{Y,X}(\lambda) \mathbf{f}^{X,X}(\lambda)^{-1} \quad (3)$$

and

$$\mathbf{f}^\eta(\lambda) = \mathbf{f}^{Y,Y}(\lambda) - \mathbf{f}^{Y,X}(\lambda) \mathbf{f}^{X,X}(\lambda)^{-1} \mathbf{f}^{X,Y}(\lambda), \quad (4)$$

where $\mathbf{f}^{X,X}(\lambda)$ and $\mathbf{f}^{X,Y}(\lambda)$ are the power and cross spectra respectively as $(q \times q)$, $(p \times p)$, $(q \times p)$, or $(p \times q)$ matrices for Y, Y , X, X , Y, X or X, Y combinations

$$\mathbf{f}^{X,Y}(\lambda) d\lambda = E(\mathbf{Z}^X(d\lambda) \mathbf{Z}^Y(d\lambda)^*) \quad (5)$$

where $\mathbf{Z}^X(d\lambda)$ being the complex Fourier amplitude of the q -dimensional vector process $\mathbf{X}(t)$. The noise spectrum can be rewritten as

$$\mathbf{f}^n(\lambda) = \mathbf{f}^{Y,Y}(\lambda)^{\frac{1}{2}} \left(\mathbf{I} - \mathbf{f}^{Y,Y}(\lambda)^{-\frac{1}{2}} \mathbf{f}^{Y,X}(\lambda) \mathbf{f}^{X,X}(\lambda)^{-1} \mathbf{f}^{X,Y}(\lambda) \mathbf{f}^{Y,Y}(\lambda)^{-\frac{1}{2}} \right) \mathbf{f}^{Y,Y}(\lambda)^{\frac{1}{2}} \quad (6)$$

which defines the coherence naturally as the fraction of $\mathbf{f}^{Y,Y}(\lambda)$ or $f^{Y,Y}(\lambda)$ for the case of $p = 1$. The coherence of $\mathbf{Y}(t)$ with $\mathbf{X}(t)$, $\rho(\lambda)$, a $(q \times q)$ matrix (100 times the sum of the Eigenvalues of $\rho^2(\lambda)$ corresponds to the percentage of power explained by $\mathbf{X}(t)$ in $\mathbf{Y}(t)$) can be calculated from the $(p \times q)$ matrix complex coherence

$$\gamma(\lambda) = \mathbf{f}^{X,X}(\lambda)^{-\frac{1}{2}} \mathbf{f}^{X,Y}(\lambda) \mathbf{f}^{Y,Y}(\lambda)^{-\frac{1}{2}} \quad (7)$$

where $\mathbf{A}^{-\frac{1}{2}}$ denotes the square root of the inverse of the Matrix \mathbf{A} , by

$$\rho_{Y,X}^2(\lambda) = \gamma(\lambda)^* \gamma(\lambda) = \mathbf{f}^{Y,Y}(\lambda)^{-\frac{1}{2}} \mathbf{f}^{Y,X}(\lambda) \mathbf{f}^{X,X}(\lambda)^{-1} \mathbf{f}^{X,Y}(\lambda) \mathbf{f}^{Y,Y}(\lambda)^{-\frac{1}{2}}. \quad (8)$$

When the $\mathbf{Y}(t)$ series is only 1-dimensional (the case we are normally dealing with), e.g. $q = 1$, expression (8) yields a scalar coherence of $Y(t)$ with $\mathbf{X}(t)$

$$\rho^2(\lambda) = \mathbf{f}^{Y,X}(\lambda) \mathbf{f}^{X,X}(\lambda)^{-1} \mathbf{f}^{X,Y}(\lambda) / f^{Y,Y}(\lambda), \quad (9)$$

or the p -dimensional partial coherence vector of $\mathbf{X}(t)$ with $Y(t)$

$$\rho^2(\lambda) = \mathbf{f}^{X,X}(\lambda)^{-\frac{1}{2}} \mathbf{f}^{Y,X}(\lambda) \mathbf{f}^{X,Y}(\lambda) / f^{Y,Y}(\lambda). \quad (10)$$

In order to get reliable estimates for the parameters they have to be smoothed; only the boxcar smoothing over $2m + 1$ elements is taken into account in the following. So all cross and power spectra become

$$\bar{\mathbf{f}}_{ZZ} = (2m - 1)^{-1} \sum_{i=-m}^{i=+m} f_Z(\lambda_j + i\Delta\lambda) \cdot f_Z^*(\lambda_j + i\Delta\lambda), \quad (11)$$

with $f_Z(\lambda_j)$ the complex amplitude at frequency λ_j ; for simplicity however we will no longer use the overbar, but assume that all power- and cross-spectra used for the calculation of the multispectral parameters are smoothed accordingly.

For the case of $q = 1$ an IDL routine has been written which calculates the transfer function with Eq. (3) and the total (Eq. 9) and partial (Eq. 8) coherence.

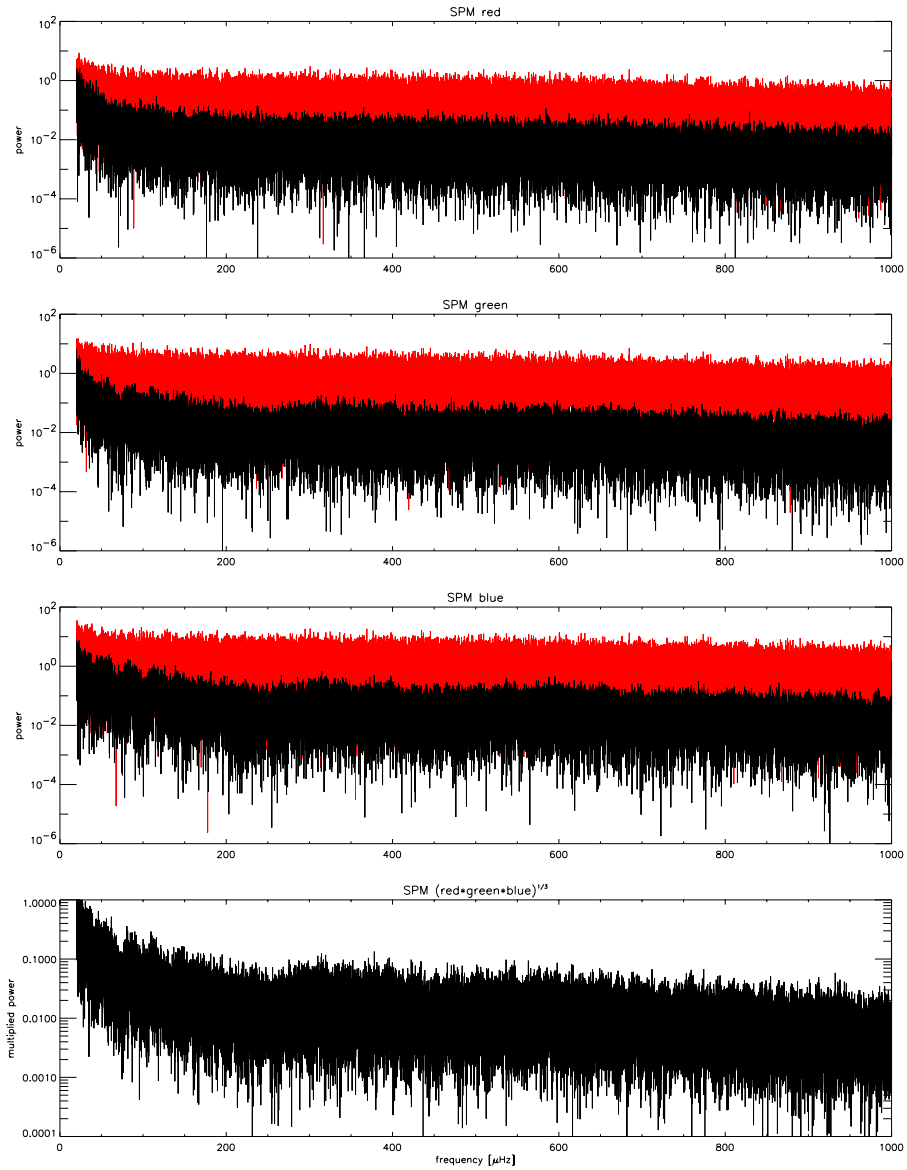


Figure 7: The top three panels show the effect of our noise reduction method on the three SPM channels red, green and blue. The original power spectra are plotted in gray, the residuals after noise reduction are plotted black. The bottom panel shows the geometric mean of the three residuals (third root of the product).

4.2 Estimation of the Uncertainties

For the estimation of the uncertainties we restrict ourselves to the case of only one timeseries Y , that is $p = 1$. For the uncertainty of the transfer function it follows

$$\left| \overline{B}_j(\lambda) - B_j(\lambda) \right|^2 \leq 2(2m+1)F_{2r,2(2m+1-r)}(\beta)(1-\rho^2) \cdot f_{YY} \cdot f_{X_j X_j}^{-1} \quad (12)$$

with $f_{X_j X_j}^{-1}$ being the diagonal elements of the inverse matrix \mathbf{f}_{XX}^{-1} and $F_{n,m}(\beta)$ the F -distribution with n, m degrees of freedom at a 100β percent confidence level. This can also be separated into gain and phase uncertainties; with

$$u_j = \left(2(2m+1)rF_{2r,2(2m+1-r)}(\beta)(1-\rho^2) \cdot f_{YY} \cdot f_{X_j X_j}^{-1} \right)^{\frac{1}{2}} \quad (13)$$

the gain has a range of

$$|A_j| - u_j \leq |A_j| \leq |A_j| + u_j \quad (14)$$

and the phase of

$$\arg A_j - \arcsin \frac{u_j}{|A_j|} \leq \arg A_j \leq \arg A_j + \arcsin \frac{u_j}{|A_j|}. \quad (15)$$

It can be shown that $\tanh^{-1} \rho$ is normally distributed, thus the coherence has the following uncertainty

$$\tanh \left(\tanh^{-1} \rho + (2m+1)^{-\frac{1}{2}} u \left(\frac{\alpha}{2} \right) \right) \leq \rho \leq \tanh \left(\tanh^{-1} \rho - (2m+1)^{-\frac{1}{2}} u \left(\frac{\alpha}{2} \right) \right) \quad (16)$$

with $u(\alpha/2)$ the upper $\alpha/2$ cutoff for the normal distribution, thus giving the $100(1-\alpha)$ percent confidence level of $\tanh^{-1} \rho$. The inverse hyperbolic tangent can be calculated by (from the definition of $\tanh(x) = (e^x - e^{-x})/(e^x + e^{-x})$)

$$\tanh^{-1} \rho = \frac{1}{2} \ln \left(\frac{1+\rho}{1-\rho} \right) \quad (17)$$

4.3 Results of Multivariate Regression Analysis of the SPM

Noise in SPM channels are very well correlated if by chance g-modes have a different correlation it is possible to enhanced their signature using a multivariate analysis.

In our example we set the time series $Y(t) = red(t)$ and $X(t) = (green(t), blue(t))$ in Eq.1 and calculate the resulting transfer functions B_{green} and B_{blue} of the corresponding fourier spectra $red(\lambda)$, $green(\lambda)$ and $blue(\lambda)$. Then the linear combination $B_{green} \times green(\lambda) + B_{blue} * blue(\lambda)$ is an estimation of $red(\lambda)$. The difference between $B_{green} \times green(\lambda) + B_{blue} \times blue(\lambda)$ and $red(\lambda)$ is then our noise reduced spectrum of the red channel. We repeated this procedure with cyclic exchanged channels. The result of the product of the three noise reduced cannels is shown in Fig. 7 together with the original and the reduced spectra for each channel.

This method allows to reduce the noise level by a factor about 100 both in g-mode and p-mode frequency range. Unfortunately for p-modes at least the correlation for modes is close to that of noise avoiding any improvement in the signal/noise ratio. Nevertheless it could be possible with this method to enhance the $l=2$ modes against $l=0$ or vice versa using the fact that limb darkening applies a different weight to these modes. It is therefore possible to produce a spectrum without $l=0$ and without $l=2$ modes. This is very useful for fitting modes especially at high frequency where the $l=0$ and $l=2$ overlap.

5 Appendix A: Kolmogorov-Smirnov test

5.1 What is Kolmogorov-Smirnov test?

The Kolmogorov-Smirnov (K-S) test is widely used to test the significance of differences between distributions of random variables. The essence of the test is in the so-called Kolmogorov-Smirnov statistics D , which is defined, for a given set of ‘observation’ x_1, x_2, \dots, x_N , as the maximum difference between the two cumulative distribution functions (cdf):

$$D \equiv \max_i |F(x_i) - S(x_i)| ,$$

where, in the case that is relevant to us, $F(x_i)$ is the ‘observed’ cdf evaluated at a data point x_i and $S(x_i)$ is the ‘theoretical’ or ‘reference’ cdf (against which $F(x)$ is tested) evaluated at the same x_i . If the observations have been sorted in ascending order, then

$$F(x_i) = i/N .$$

Then one calculates the probability of observing D equal to, or greater than, the observed value when the true cdf is $S(x)$ *i.e.*, the likelihood of $S(x)$ being the true cdf given the observation. For large sample size N , this probability is approximately $Q_{KS}(\sqrt{ND})$, where the function Q_{KS} is given by the formula

$$Q_{KS}(\lambda) = 2 \sum_{j=1}^{\infty} (-1)^j e^{-2\lambda^2 j^2}$$

(see, *e.g.*, *Nonparametric Statistical Methods*, Hollander & Wolfe 1973, Wiley & Sons), which clearly is very slowly converging for small λ , and in fact diverges for $\lambda = 0$. However, with decreasing λ , $Q_{KS}(\lambda)$ approaches unity much quicker than the formula becomes a nuisance. For any precision that is of practical use, one needs to use the formula only in the range, say, $0.1 \leq \lambda \leq 6$, below which and above which we can set $Q_{KS}(\lambda)$ to be unity and zero respectively. Indeed, this is what is done in the IDL routine TS has provided.

5.2 The possible relevance of the K-S test to the g-mode search

Generally speaking, the K-S test can be used to test if there is anything in the stochastic signal that deviates from what we expect statistically. In principle, it can be used to test whether, say, power spectrum in certain frequency range can be explained by known sources of (solar and instrumental) noise. If it is not, then there is something not understood, which may or may not be g modes. However it should be noted that, even if we somehow know that g-mode signal is there, actually to *find* peaks that are of g-mode origin is entirely a different story.

One of the strategy adopted for the g-mode search was to look at cross spectra between LOI and MDI,

$$F_{\text{cross}}(\nu) = F_{\text{LOI}}(\nu)F_{\text{MDI}}^*(\nu) .$$

If the two Fourier spectra are statistically totally dependent, then this quantity is of no interest. The K-S test can also be used to test their independence.

5.3 What was done before 3 Nov

DOG and TS wrote down an IDL routine to compute the cdf of product of two independent standard gaussians. First, the probability distribution function (pdf) was calculated, which was found (by DOG) to be related to a modified Bessel function but still had to be evaluated numerically. The pdf was then numerically integrated to obtain cdf. Since the K-S test of the datasets would require evaluation of cdf at a huge number of points, it was decided that the result be tabulated so that the cdf can be evaluated by interpolation (inside IDL). TS also wrote down IDL routines for K-S test for general case, so that various datasets can be tested against various cdfs.

5.4 What was done during 3–7 Nov

ThA and TS looked at the LOI-MDI cross spectra for various sets of (l, m) . The first thing ThA noticed was that for $l = 1, m = 0$, the statistics of the cross spectrum in p-mode range (but away from peaks) were not consistent with that of products of two independent gaussians. How to interpret this we do not know — had ThA checked if individual spectra were consistent with gaussian statistics?

The results of the K-S test at g-mode range tended to be one of two extremes, the statistics of cross spectra at various range having been either highly consistent (likelihood very high) or totally inconsistent (likelihood very low) with the hypothesis of independent gaussians. One difficulty was in the subtraction of the background; with varying background noise, irrespective of the presence of g modes, for sufficiently wide range of frequencies the K-S test is bound to reject the hypothesis of independent gaussians if one does not do some detrending, or one does not do detrending properly. So, when one gets very low likelihood for independent gaussians, one does not know if this is because holy grails are lurking or because detrending has not been done properly.

Artificial data were also tested with disappointing results (or so we thought at the time). The data were created by adding peaks to artificially generated

background noise, and then the K-S test was applied to see if it would ‘detect’ the presence of peaks. It did so only when the S/N ratio is higher than unity, or when the number density of peaks are high. This was partly due to the fact that g-mode peaks did not occupy too many frequency bins, because it was (probably correctly) assumed that the g-mode peaks were very sharp. The case where g-mode peaks occupy more than one bin was not tested, but provided that the peak heights are maintained (that is to say the total power in peaks are increased), it would certainly make the ‘detection’ easier.

The cross spectrum between whole disk measurements (one of them might be a proxy), where the number density of g-mode peaks would be high, was not tested. Perhaps one should try this. Also, the low frequency p-mode range was not tested with this method.

One aspect that was sometimes ignored, in a way, was the fact that the cross spectrum is a complex quantity. The IDL routine ThA had setup (accommodating TS’s K-S routines) carried out tests for the products of real/imaginary part of one spectrum and real/imaginary part of the other (there are four combinations), which should be combined to yield the statistics for cross spectrum but sometimes we did not bother.

To summarize, the picture is not exceedingly rosy but there is a feeling that this was just the beginning and we did not do things quite properly. One has to bear in mind that a test is a test and nothing more, but we may eventually benefit from trying a bit harder along this line.

6 Appendix B: Mode frequencies

Table 1: Mode frequency for Nice model (S13-I-4406). $l = 0, 1$

l	mode type- n	Frequency (in μHz)	Splitting (in nHz)
0	p1	257.61	
0	p2	403.93	
0	p3	535.38	
0	p4	680.17	
0	p5	825.09	
0	p6	972.59	
0	p7	1118.05	
0	p8	1263.44	
0	p9	1407.59	
0	p10	1548.44	
0	p11	1686.77	
0	p12	1822.23	
0	p13	1957.49	
1	g5	107.67	212.
1	g4	125.96	210.
1	g3	151.26	210.
1	g2	189.00	213.
1	g1	259.75	242.
1	p1	284.21	396.
1	p2	448.31	433.
1	p3	596.84	429.
1	p4	746.56	427.
1	p5	893.63	427.
1	p6	1039.45	428.
1	p7	1185.59	428.
1	p8	1329.69	429.
1	p9	1473.00	430.
1	p10	1612.83	430.
1	p11	1749.48	431.
1	p12	1885.26	431.

Table 2: Mode frequency for Nice model (S13-I-4406). $l = 2$

l	mode type- n	Frequency (in μHz)	Splitting (in nHz)
2	g10	100.97	365.
2	g9	110.12	365.
2	g8	120.85	365.
2	g7	133.68	363.
2	g6	149.29	360.
2	g5	168.36	354.
2	g4	191.70	346.
2	g3	219.75	345.
2	g2	253.54	373.
2	g1	293.89	409.
2	f	352.14	366.
2	p1	382.44	348.
2	p2	514.29	391.
2	p3	664.34	411.
2	p4	811.71	420.
2	p5	959.85	425.
2	p6	1105.12	427.
2	p7	1250.67	430.
2	p8	1394.67	431.
2	p9	1535.91	432.
2	p10	1674.66	433.
2	p11	1810.32	434.
2	p12	1945.89	434.

Table 3: Mode frequency for Nice model (S13-I-4406). $l = 3$

l	mode type- n	Frequency (in μHz)	Splitting (in nHz)
3	g14	102.42	400.
3	g13	109.07	401.
3	g12	116.57	401.
3	g11	125.06	401.
3	g10	134.89	401.
3	g9	146.32	401.
3	g8	159.55	401.
3	g7	175.08	400.
3	g6	193.49	396.
3	g5	214.69	385.
3	g4	236.20	373.
3	g3	258.90	399.
3	g2	293.06	416.
3	g1	336.68	422.
3	f	392.17	406.
3	p1	415.66	384.
3	p2	564.60	403.
3	p3	718.47	416.
3	p4	866.94	423.
3	p5	1015.00	427.
3	p6	1161.72	429.
3	p7	1306.79	432.
3	p8	1451.09	433.
3	p9	1591.56	434.
3	p10	1729.20	436.
3	p11	1865.30	436.
3	p12	2001.16	436.

Table 4: Mode frequency for Nice model (S13-I-4406). $l = 4$

l	mode type- n	Frequency (in μHz)	Splitting (in nHz)
4	g18	102.74	414.
4	g17	107.89	414.
4	g16	113.54	414.
4	g15	119.77	414.
4	g14	126.73	414.
4	g13	134.54	415.
4	g12	143.27	415.
4	g11	153.08	415.
4	g10	164.29	416.
4	g9	177.25	416.
4	g8	192.06	416.
4	g7	209.13	415.
4	g6	228.85	410.
4	g5	248.51	385.
4	g4	262.89	398.
4	g3	288.16	422.
4	g2	324.09	424.
4	g1	364.64	429.
4	f	410.83	420.
4	p1	441.54	397.
4	p2	603.20	414.
4	p3	761.13	423.
4	p4	913.21	427.
4	p5	1062.11	431.
4	p6	1210.60	432.
4	p7	1356.37	434.
4	p8	1500.41	436.
4	p9	1641.00	436.
4	p10	1778.10	437.
4	p11	1914.83	438.

Table 5: Mode frequency for Nice model (S13-I-4406). $l = 5$

l	mode type- n	Frequency (in μHz)	Splitting (in nHz)
5	g22	102.77	420.
5	g21	106.95	420.
5	g20	111.46	420.
5	g19	116.36	421.
5	g18	121.70	421.
5	g17	127.54	421.
5	g16	133.92	421.
5	g15	140.92	421.
5	g14	148.68	421.
5	g13	157.34	422.
5	g12	166.95	422.
5	g11	177.66	422.
5	g10	189.77	423.
5	g9	203.63	423.
5	g8	219.29	423.
5	g7	237.08	422.
5	g6	257.18	417.
5	g5	271.06	380.
5	g4	285.13	422.
5	g3	312.71	427.
5	g2	346.63	428.
5	g1	381.86	431.
5	f	420.57	425.
5	p1	467.75	407.
5	p2	637.84	421.
5	p3	798.92	428.
5	p4	954.33	430.
5	p5	1104.88	433.
5	p6	1254.57	435.
5	p7	1401.64	436.
5	p8	1545.32	437.
5	p9	1685.97	438.
5	p10	1823.40	438.
5	p11	1960.61	439.

Table 6: Mode frequency for Nice model (S13-I-4406). $l = 6$

l	mode type- n	Frequency (in μHz)	Splitting (in nHz)
6	g25	106.23	424.
6	g24	109.99	424.
6	g23	114.00	424.
6	g22	118.31	424.
6	g21	122.96	424.
6	g20	127.95	424.
6	g19	133.35	425.
6	g18	139.21	425.
6	g17	145.60	425.
6	g16	152.55	425.
6	g15	160.13	425.
6	g14	168.48	425.
6	g13	177.73	426.
6	g12	187.93	426.
6	g11	199.20	426.
6	g10	211.82	426.
6	g9	226.13	426.
6	g8	242.11	427.
6	g7	260.04	427.
6	g6	280.09	421.
6	g5	288.25	387.
6	g4	305.29	428.
6	g3	331.93	429.
6	g2	362.97	430.
6	g1	393.00	432.
6	f	426.74	427.
6	p1	493.12	415.
6	p2	670.05	425.
6	p3	834.21	431.
6	p4	992.27	433.
6	p5	1145.00	435.
6	p6	1295.54	437.
6	p7	1443.77	437.
6	p8	1587.46	438.
6	p9	1727.86	439.
6	p10	1866.15	439.

Table 7: Mode frequency for GONG model computed at Nice. $l = 0, 1$

l	mode type- n	Frequency (in μHz)	Splitting (in nHz)
0	p1	258.01	
0	p2	404.48	
0	p3	535.94	
0	p4	680.57	
0	p5	825.36	
0	p6	972.74	
0	p7	1118.15	
0	p8	1263.51	
0	p9	1407.62	
0	p10	1548.51	
0	p11	1686.80	
0	p12	1822.21	
0	p13	1957.45	
1	g5	109.27	214.
1	g4	127.89	212.
1	g3	153.39	211.
1	g2	191.88	214.
1	g1	262.98	253.
1	p1	285.11	385.
1	p2	448.47	433.
1	p3	596.94	429.
1	p4	746.66	427.
1	p5	893.71	427.
1	p6	1039.56	428.
1	p7	1185.62	428.
1	p8	1329.69	429.
1	p9	1472.97	430.
1	p10	1612.72	430.
1	p11	1749.38	431.
1	p12	1885.09	431.

Table 8: Mode frequency for GONG model computed at Nice. $l = 2$

l	mode type- n	Frequency (in μHz)	Splitting (in nHz)
2	g10	102.60	365.
2	g9	111.85	365.
2	g8	122.75	364.
2	g7	135.74	363.
2	g6	151.48	359.
2	g5	170.70	353.
2	g4	194.36	345.
2	g3	222.32	346.
2	g2	256.51	376.
2	g1	296.53	408.
2	f	355.78	361.
2	p1	384.16	352.
2	p2	514.47	391.
2	p3	664.40	411.
2	p4	811.76	420.
2	p5	959.87	425.
2	p6	1105.17	427.
2	p7	1250.72	430.
2	p8	1394.70	431.
2	p9	1535.98	432.
2	p10	1674.67	433.
2	p11	1810.27	434.
2	p12	1945.81	434.

Table 9: Mode frequency for GONG model computed at Nice. $l = 3$

l	mode type- n	Frequency (in μHz)	Splitting (in nHz)
3	g14	104.13	400.
3	g13	110.85	401.
3	g12	118.46	401.
3	g11	127.12	401.
3	g10	137.05	401.
3	g9	148.58	401.
3	g8	162.01	401.
3	g7	177.72	399.
3	g6	196.24	395.
3	g5	217.34	384.
3	g4	238.68	374.
3	g3	261.65	402.
3	g2	296.84	416.
3	g1	340.11	422.
3	f	396.98	403.
3	p1	416.35	386.
3	p2	564.71	403.
3	p3	718.51	416.
3	p4	866.95	423.
3	p5	1015.01	427.
3	p6	1161.69	429.
3	p7	1306.79	432.
3	p8	1451.05	433.
3	p9	1591.54	434.
3	p10	1729.20	436.
3	p11	1865.24	436.
3	p12	2001.08	436.

Table 10: Mode frequency for GONG model computed at Nice. $l = 4$

l	mode type- n	Frequency (in μHz)	Splitting in nHz
4	g18	104.46	414.
4	g17	109.68	414.
4	g16	115.42	414.
4	g15	121.77	414.
4	g14	128.82	415.
4	g13	136.70	415.
4	g12	145.56	415.
4	g11	155.55	415.
4	g10	166.90	416.
4	g9	179.93	416.
4	g8	194.94	416.
4	g7	212.22	414.
4	g6	231.93	408.
4	g5	250.62	382.
4	g4	265.42	404.
4	g3	291.73	422.
4	g2	328.39	424.
4	g1	368.25	429.
4	f	416.24	420.
4	p1	441.66	397.
4	p2	603.23	414.
4	p3	761.14	423.
4	p4	913.17	427.
4	p5	1062.09	431.
4	p6	1210.52	432.
4	p7	1356.29	434.
4	p8	1500.34	436.
4	p9	1640.89	436.
4	p10	1778.01	437.
4	p11	1914.71	438.

Table 11: Mode frequency for GONG model computed at Nice. $l = 5$

l	mode type- n	Frequency (in μHz)	Splitting (in nHz)
5	g22	104.51	420.
5	g21	108.74	420.
5	g20	113.33	420.
5	g19	118.30	421.
5	g18	123.71	421.
5	g17	129.63	421.
5	g16	136.11	421.
5	g15	143.23	421.
5	g14	151.10	421.
5	g13	159.83	422.
5	g12	169.57	422.
5	g11	180.47	422.
5	g10	192.73	423.
5	g9	206.65	423.
5	g8	222.51	423.
5	g7	240.52	422.
5	g6	260.41	413.
5	g5	272.20	383.
5	g4	288.63	424.
5	g3	316.66	427.
5	g2	351.14	428.
5	g1	385.46	431.
5	f	426.19	424.
5	p1	467.80	407.
5	p2	637.83	421.
5	p3	798.90	428.
5	p4	954.25	430.
5	p5	1104.81	433.
5	p6	1254.49	435.
5	p7	1401.51	436.
5	p8	1545.23	437.
5	p9	1685.84	438.
5	p10	1823.21	438.
5	p11	1960.44	439.

Table 12: Mode frequency for GONG model computed at Nice. $l = 6$

l	mode type- n	Frequency (in μHz)	Splitting (in nHz)
6	g25	108.02	424.
6	g24	111.83	424.
6	g23	115.91	424.
6	g22	120.28	424.
6	g21	124.99	424.
6	g20	130.06	424.
6	g19	135.55	425.
6	g17	147.96	425.
6	g16	155.00	425.
6	g15	162.71	425.
6	g14	171.17	425.
6	g13	180.50	425.
6	g12	190.83	426.
6	g10	215.06	426.
6	g9	229.41	426.
6	g8	245.58	427.
6	g7	263.74	427.
6	g6	283.28	427.
6	g5	289.19	413.
6	g4	309.16	395.
6	g3	336.04	428.
6	g2	367.57	429.
6	g1	396.56	430.
6	f	432.52	432.
6	p1	493.15	427.
6	p2	670.02	415.
6	p3	834.18	425.
6	p4	992.18	431.
6	p5	1144.88	433.
6	p6	1295.42	435.
6	p7	1443.61	437.
6	p8	1587.31	437.
6	p9	1727.71	438.
6	p10	1865.91	439.